Defense Threat Reduction Agency
8725 John J. Kingman Road, Stop 6201
Fort Belvoir, VA 22060-6201

DTRA-TR-24-10

TECHNICAL REPORT

# A Combined Experimental, Theoretical and Computational Approach to the Interaction of Prompt X-rays with Solar Panels

15 December 2023

PI: Dr. Simon Bland, Email: sn.bland@imperial.ac.uk

Imperial College London

# REPORT DOCUMENTATION PAGE

*Form Approved*
*OMB No. 0704-0188*



| **1. REPORT DATE** *(DD-MM-YYYY)* | **2. REPORT TYPE** | **3. DATES COVERED** *(From - To)* |
|---|---|---|
| 12/15/2023 | Final Report | 02/01/2020-07/31/2023 |

**4. TITLE AND SUBTITLE**
A combined experimental, theoretical and computational approach to the interaction of prompt X-rays with solar panels

**5a. CONTRACT NUMBER**

**5b. GRANT NUMBER**
HDTRA1-20-1-0001

**5c. PROGRAM ELEMENT NUMBER**

**6. AUTHOR(S)**
Simon Bland[1], Jeremy Chittenden[1], Aidan Crilly[1], Jack Halliday[1], Sergey Lebedev[1], Roberto Mancini[2], Stefano Merlini[1], Steve Rose[1], and Danny Russell[1]
[1] Imperial College London, [2] University of Nevada, Reno

**5d. PROJECT NUMBER**

**5e. TASK NUMBER**

**5f. WORK UNIT NUMBER**

**7. PERFORMING ORGANIZATION NAME(S) AND ADDRESS(ES)**
**AND ADDRESS(ES)**
**Imperial College London**
**South Kensington Campus**
**London SW7 2AZ, UK**

**8. PERFORMING ORGANIZATION REPORT NUMBER**

**9. SPONSORING / MONITORING AGENCY NAME(S) AND ADDRESS(ES)**
Defense Threat Reduction Agency/RD-NTS
8725 John J. Kingman Rd., MSC 6201
Ft. Belvoir, VA 22060-6201

**10. SPONSOR/MONITOR'S ACRONYM(S)**
DTRA/RD-NTS

**11. SPONSOR/MONITOR'S REPORT NUMBER(S)**
DTRA-TR-##-##

**12. DISTRIBUTION / AVAILABILITY STATEMENT**
Cleared for Public Release

**13. SUPPLEMENTARY NOTES**

**14. ABSTRACT**
We aim to utilize a pulsed power radiation platform to provide detailed quantitative data on the physical processes underlying the interaction of soft 'prompt' X-rays with solar panel materials and structures across a wide range of intensities. The measurements are then be used to develop accurate theory and large-scale simulations of these effects.

**15. SUBJECT TERMS**
Exo-atmospheric nuclear burst, cold X-rays, satellite's materials, solar cell panels, warm dense plasma, blow-off, dense plasma composition, optical and electrical properties, radiative transfer in plasmas

| **16. SECURITY CLASSIFICATION OF:** | | | **17. LIMITATION OF ABSTRACT** | **18. NUMBER OF PAGES** | **19a. NAME OF RESPONSIBLE PERSON** |
|---|---|---|---|---|---|
| **a. REPORT** | **b. ABSTRACT** | **c. THIS PAGE** | Unclassified | **38** | Jacob Calkins |
| Unclassified | Unclassified | Unclassified | | | **19b. TELEPHONE NUMBER** *(include area code)* (571) 616-5946 |

**HDTRA1-20-1-0001**

# A combined experimental, theoretical and computational approach to the interaction of prompt X-rays with solar panels

**PIs: Dr Simon Bland**

**Co-I: S.V. Lebedev, J.P. Chittenden, S. Rose, R. Mancini**

**November 2023 (with minor additions/edits Jan 2024)**

**Project manager: Jacob Calkins**

**Final Report for DTRA project**

## TABLE OF CONTENTS

**Section** **Page**

## CONTIBUTING AUTHORS

Simon Bland[1], Jeremy Chittenden[1], Aidan Crilly[1], Jack Halliday[1], Sergey Lebedev[1], Roberto Mancini[2], Stefano Merlini[1], Steve Rose[1], and Danny Russell[1]

[1] Imperial College London, [2] University of Nevada, Reno.

## 1.0 INTRODUCTION

The network of satellites employed by the US is vital for the security and defence of America and its allies. One of the greatest concerns is the susceptibility of these satellites to attack, particularly from the effects of high altitude/exo-atmospheric nuclear weapons. As 'rogue nations' continue to develop these weapons and produce suitable delivery vehicles, the problem has become more pressing, and there is a need to ensure that the potential effect on the satellite network is both quantified and – if possible – countered through better design.

Some of the effects of high altitude nuclear detonations are well known; particularly their ability to produce highly energetic particles which can be trapped by the Earths magnetic field and degrade/destroy the electronics in satellites even for many days after the explosion[1]. In close proximity to a detonation the X-rays produced can ablate the satellites casing, launching strong shock waves into the structure and damaging internal components through spalling. One effect that is less well known is the interaction of relatively soft 'prompt' X-rays with the solar panels that now power most of the satellites.

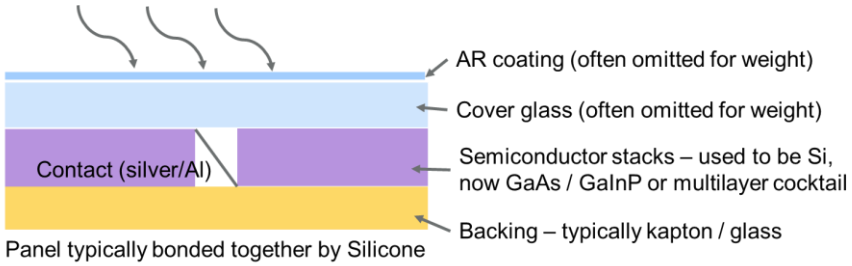


*Fig. 1 A cross section of a simple solar panel, for illustrative purposes*

At first consideration the interaction of soft X-rays with solar panels appears simple – the X-rays will penetrate the panels to an absorption depth; and the deposited energy will boil/ablate material in the panel forming a plasma. In reality, however, it will likely depend strongly on the intensity and wavelength of the X-rays involved and the construction of the solar panel (Fig. 1). To illustrate the problem, we can consider a weapon of 1MT yields. If say 10% of the energy is converted into soft X-rays, over a duration of between 10 and 100ns, then the solar panels of a satellite at 1 km from detonation would experience ~3kJ/cm$^2$ and intensities of 30-300GW/cm$^2$ ; at 1000km this drops to ~3mJ/cm$^2$ with intensities 30-300kW/cm$^2$.

At the top end this is similar to the intensities that can be made in many laser-solid interaction experiments (albeit to typically much smaller scales with focused laser systems); and indeed the solar panel is expected to ablate. Close to the panel conditions often referred to as 'warm dense matter' will dominate, this cross over between condensed matter and plasma physics is extremely difficult to model as the plasmas formed are still closely coupled. For weight and cost considerations solar panels in many satellites are left bare, with no cover glass or protection/potting of the contacts joining adjacent cells in the panel, hence plasma from the cells themselves and any backing material could effectively fills the gaps between any cells, shorting these if its conductivity is high enough, coupling differently biased solar cells to each other, to

spacecraft structures, or to the space plasma itself, with subsequent electrical affects causing catastrophic damage to the satellites systems. As material starts to ablate from the panel and become ionised, it too will absorb incoming X-rays and heat up, and thermal transport from this plasma to the panel could play a factor in determining how ablation continues. In extreme cases, shocks launched through the panels could damage the structure of the panel itself or even change the phase of the material, significantly altering the material properties - silicon, for instance, undergoes an insulator-metal transitions at ~13GPa.

As we move further from the detonation intensities rapidly drops, and ablation issues less likely. However soft X-rays could still produce photo-electrons at the solar panel, and with high enough intensity, and large enough voltages on the panel enough photoelectrons could be produced to initiate a conducting arc between adjacent cells, again causing significant electrical damage. Again this process is very difficult to model, and experimental data is limited at the large (mm-cm) scales associated with solar panel structures due to the difficulties in producing intense bursts of soft X-rays over such areas. Hence the precise effects of low intensity bursts of soft X-rays on solar panels are relatively unknown, and methods to counter these bursts underdeveloped.

Given that in Low Earth Orbit satellites may be 50-100km apart this issue, 1 nuclear detonation might effectively damage a very large number satellites. It is clear that we must obtain quantitative data on the effects of soft X-ray bursts on solar panel materials subject under a wide range of representative intensities / energy depositions; and then to utilize this new data to produce and refine both theory and computational modelling of the situation. Only then can we truly understand the likely effects of a nuclear detonation on a network of satellites, and explore cost effective defenses.

## 2.0 METHODS FOR PRODUCING SOFT X-RAY BURSTS – THE USE OF PULSED POWER

There are several ways in which bursts of such soft X-rays could be produced. For example 3rd generation synchrotrons can readily make broad band emission in the correct spectral range and could illuminate targets at the lowest fluencies; however the pulse length from synchrotrons is generally short (ns) and with large facilities come cost/access time issues. This is especially true as the different diagnostic techniques needed to make measurements of the ablating plasma at the panels will take multiple experiments to optimise. Alternately lasers can be focussed onto high-Z targets/into hohlraums to produce the required spectra; but in this case the required fluences and durations will necessitate the use of lasers with very high energies, again limiting experiments to large scale facilities - indeed the Omega laser facility is where some of the first measurements of the effects of soft X-rays on solar panel materials have been made.

In comparison to lasers and synchrotrons, pulsed power driven z-pinch implosions – particularly those from wire array z-pinches - offer a set of advantages. Developed for the ICF program, the implosion of a wire array z-pinch produces high yield pulses of X-ray radiation, controllably, repeatable and with high efficiencies. On large facilities such as the Z generator at Sandia National Labs, this technique has produced KJ pulses of K-shell radiation and MJ bursts of soft blackbody radiation for ICF purposes . Much of the research into the fundamental behaviour of wire arrays though was carried out on university based pulsed power facilities, such as the MAGPIE facility at Imperial College. Even with much smaller currents (1MA on MAGPIE vs 26MA on Z) KJ yields of soft radiation are still produced at this scale – a level ideal for exploring the effects of X-rays on solar panels. Further experimental work in ICF, particularly wire array Z-pinches at the universities often occurred simultaneously to the creation and development of large scale MHD / RMHD codes, that are well suited to model the effects of radiation on solar panels.

### 2.1 Objectives of the project

We aim to utilize a pulsed power radiation platform to provide detailed quantitative data on the physical processes underlying the interaction of soft ‘prompt’ X-rays with solar panel materials and structures across a wide range of intensities. The measurements are then be used to develop accurate theory and large scale simulations of these effects.

## 3.0 EXPLORING THE EFFECT OF X-RAY RADIATION ON SOLAR CELL MATERIALS WITH A PULSED POWER PLATFORM

In a wire array z-pinch, cylindrical arrays of fine metallic wires are subject to mega-ampere level currents with risetimes of ~100-300ns. The wires rapidly heat and expand forming cold dense wire cores that ablate into warm, low density coronal plasma. Current flowing through this plasma interacts with the induced magnetic field and accelerates the plasma towards the axis. As ablation continues the wire cores start to run out of mass, and the implosion of the array begins[2]. This proceeds to snowplough though the ablated material before arriving on axis, where it stagnates emitting X-rays. The accumulation of material during the implosion phase has a stabilising effect resulting in very short pulse/fast risetime of X-ray emission[3,4] (Fig. 2)

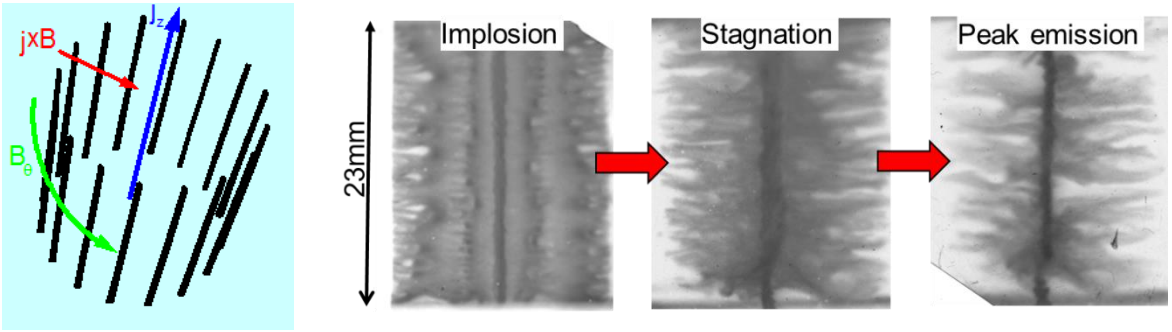


*Fig. 2 Left, schematic of cylindrical wire array z-pinch showing wires subject to a large, fast rising current. The wires ablate and implode due to the JxB force. Right, 3 sequential XUV framing images showing the implosion and stagnation of an aluminium wire array on MAGPIE.*

Changing the material of the wires will alter the spectrum emitted. With low Z wires like aluminium, emission at stagnation is predominantly from the K-shell lines together with a non-thermal continuum that stretches over a wide band of energies. Using wires of higher atomic number results in a large huge number of closely packed emission lines that tend to form more of a quasi-broadband, cooler blackbody spectrum. The duration of the X-ray pulse can also be readily altered. The very shortest pulses available through pulsed power driven implosions use 'X-pinch' loads[5] to produce single points of highly unstable, rapidly imploding plasmas - resulting in sub ns pulses. Alternately, using conical arrays produces zippered implosions[6] that stretch out the X-ray pulse in time to many 10s of ns (fig. 3).

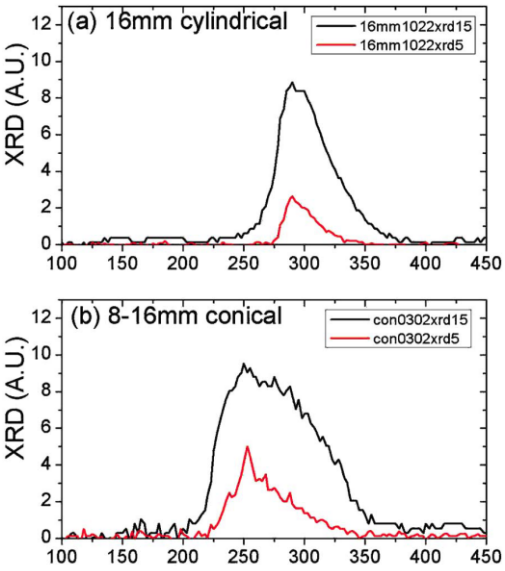


*Fig. 3 Above, simulations of the zippered implosion of a conical array made by the 3D MHD Gorgon codes. Right: Soft X-ray emission from the conical array compared to a cylindrical array, demonstrating that the X-ray emission is extended in time*

### 3.1 'High Flux' Experiments

The MAGPIE facility at Imperial College produces currents up to 1.4MA with rise times ~ 240ns rise-times. The arrays we used for this work were typically designed to implode near the peak of the current pulse (providing the highest efficiency X-rays production) with 32 x 13μm aluminum wires on a 16 mm diameter, and a height of 20mm. The X-ray yield from the pinch at stagnation is 10-20kJ, over a FWHM of ~25ns. This gives a power output of 0.4 - 0.8 TW, the vast majority of which is as soft X-rays (<1keV), with harder KeV emission accounting for <1%.

Our initial setup utilized simple Silicon targets and was designed to leverage the established suite of optical diagnostics available for experiments on MAGPIE[7]. These diagnostics were all directed onto the axis of MAGPIE's pre-existing vacuum chamber, which also houses the wire array z-pinch. As such, the maximum distance between the array and the target was limited to ~40mm. The Silicon targets were planar slabs with a face 10x10 mm and a thickness of 0.5mm and were arranged to directly face the axis of the array.

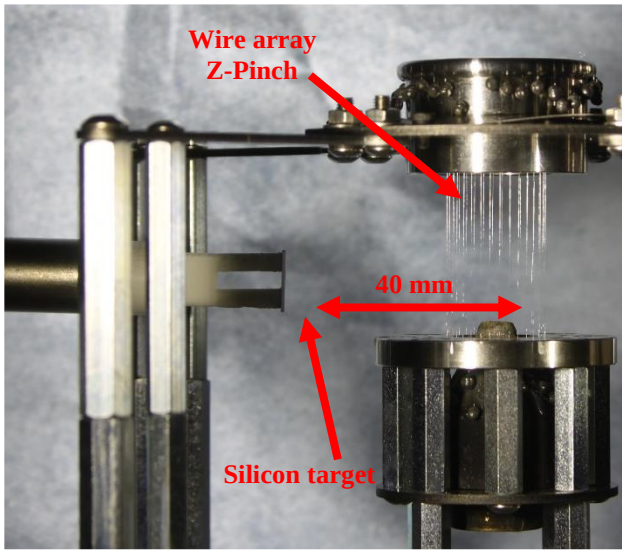


*Fig. 4 is a setup photo for a typical experiment. It shows the wire array supported on stainless steel current carrying rods, and the silicon slab which is supported by a holder made from 3D printed plastic.*

On the axis of the array, the stagnating plasma typically emits from a cylinder ~1mm in diameter. The driving X-Rays are emitted from each point of the surface of this cylinder and radiate into $2\pi$ steradians. This means that only a fraction of the X-Ray flux impinges on the silicon slab - an effect called geometry dilution. We have modeled the geometry dilution effect for the Magpie silicon ablation experiment using the view-factor code VISRAD[8] taking into the size and shape of the z-pinch radiation source and silicon target, and the distance between them.

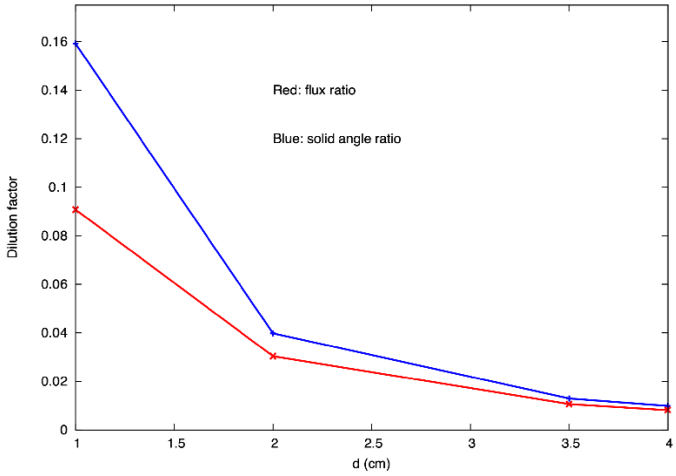


| d (cm) | Flux ratio |
|---|---|
| 1.0 | 0.0908 |
| 2.0 | 0.0304 |
| 3.5 | 0.01066 |
| 4.0 | 0.00820 |

*Fig. 5: A plot of dilution factor as a function of pinch-to-target distance, calculated using the view factor code VISRAD.*

Fig. 5 displays the geometry dilution factor computed with VISRAD (red) as well as an approximation based on the average solid angle subtended by the silicon slab target as seen from the z-pinch source (blue) as a function of the source-target distance d. The geometry dilution effect is significant; for the Magpie experimental configuration with d=3.5cm only 1% of the x-ray flux at the source actually reaches the silicon target.

The dynamics of a wire array z-pinch are, however, slightly more complicated. Rather than implode as a shell like annulus of plasma, the wires in the array initially form core-corona plasma systems with cold, relatively dense wire cores being slowly ablated into hot, low density coronal plasma. Current initially remains concentrated close to the wire cores, where it acts to project the coronal plasma towards the axis. Here it forms a precursor column of plasma, that itself emits soft X-rays - in this case though at a much lower level 10s – 100s J over ~100ns (a few GW in power). Only when the wire cores start to run out of mass does current then transfer to the bulk of the array material, rapidly accelerating this onto the precursor column to give the large X-ray pulse observed at stagnation[2,3]. Hence taking into account the dilution we expect that at the target radiation from the:

- Precursor contributes a yield up to ~ 8J/cm$^2$, rising in intensity from ~120ns to ~0.1GW/cm$^2$ just prior to stagnation
- Main pulse contributes a yield up to ~ 400J/cm$^2$ over 25ns at stagnation – an average intensity ~10GW/cm$^2$

We note that the main pulse is expected to produce similar intensities / yields on the Silicon target as might be expect if a satellite was within a few km of a 1MT nuclear detonation; whilst the precursor could be better associated with smaller yields / distances in the 10-100km region.

*(Aside: Magnetic fields*
We note that in this configuration any plasma outflow from irradiation of the Silicon target will expand into a magnetic field ~ 10 T (as the current flowing through the z-pinch is in close proximity to the target). Clearly such a strong magnetic field could not be generated in the vicinity of a solar panel. That said, the presence of the field in the experiments is an asset because it can be used as a tracer to explore resistivity in the ablated plasma outflow)

***Results and discussion***

Measurements of the conditions of ablated plasma outflows were made using interferometry, self-emission imaging, optical Thomson scattering, and Faraday rotation imaging. Fig. 6 shows a typical interferogram, obtained in an experiment with a separation of 20 mm between the silicon target and the Z-pinch. In the image, the deviation of interference fringes from their position in the absence of plasma provides information about line integrated electron density. The interferogram shows the initial position of the target as a white mask (behind X=0 mm) In the region between X=0 mm and 2 mm, the plasma is dense enough to absorb the probing laser beam and so interference fringes are lost. In the region X = 2 – 4 mm, fringes are observed and so a measurement of electron density can be made. The signature of the stagnated wire array Z-Pinch (our source of driving X-Rays) can also be seen and is centered on X = 20 mm.

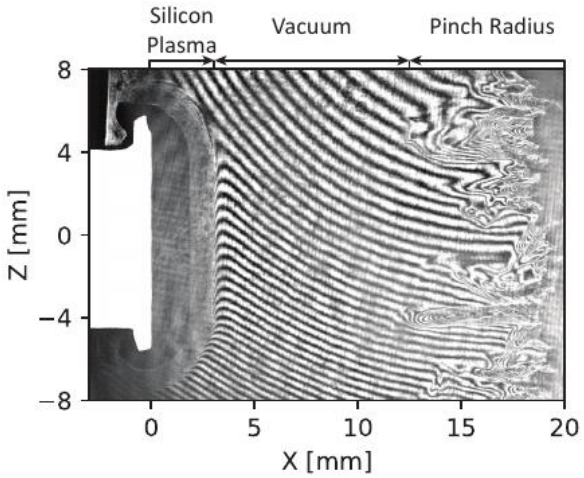


*Fig. 6: An interferogram captured in an X-Ray driven silicon ablation. In the image we see plasma ablated from the target in the region* $0 < X < 4\ mm$*, and plasma from the wire array Z-pinch in the region* $12 < X < 20\ mm$*.*

From this interferometry data, a striking finding is that the density profile of the outflow is near constant at all Z positions. In some experiments, simultaneous laser probing was carried out in the orthogonal direction (probing along Z with resolution in the X, Y plane). This revealed a similar degree of uniformity in the Y direction - suggesting a quasi-1D profile of expanding plasma.

Fig. 7 shows the emission front of plasma expanding from the target captured using a fast-framing camera. The plot shows front trajectories from three separate experiments. For the data labelled s0618_20 blue triangles, the separation between the pinch and the silicon target was 20 mm. The data in s0908_20 (red circles) used the same wire array z-pinch source but the array to target separation was increased to 40 mm. The data labelled s0703_20 (light pink squares) again used 20mm array to target separation but now the wires in the Z-pinch were significantly over-massed to prevent implosion - so only radiation from a precursor plasma illuminated the target.

Comparisons between self-emission images and interferometry data (captured along the same line of sight) reveal that the positions measured using self-emission sit some-way behind the density front measured with interferometry, but they can still provide a useful insight into the dynamics of the experiments. In particular, Fig. 7 also shows the trace from a Beryllium filtered PCD detector which was fielded in all three experiments. This diagnostic is sensitive to X-Rays above around 700 eV and these are only produced after implosion. It is evident that the velocity of the ablation front increases at the time of implosion in both s0618_20 and s0908_20. After the Z-Pinch X-rays switch off, the velocity of the front remains constant for the duration of the period which was diagnosed. In s0618_20 (20 mm target separation) the measured front velocity is $4.3 \pm 0.1 \times 10^6\ \mathrm{cm/s}$. In s0908_20 (40 mm target separation) the velocity was reduced to $3.3 \pm 0.1 \times 10^6\ \mathrm{cm/s}$. Comparing multiple experiments the velocity appears to scales as $v \propto 1/\sqrt{(d)}$, which is consistent with a coupling of X-Ray energy into plasma kinetic energy, given that the pinch acts as a line source at small target separations.

Prior to implosion, s0618_20 and s0908_20 both follow a similar trajectory to s0703_20, with a measured front velocity of $1.3 \pm 0.1 \times 10^6\ \mathrm{cm/s}$ At early times for all three experiments, and for the entire duration of s0703_20, the driving radiation field is dominated by emission from the 'precursor' column of ablated plasma on the central axis of the pinch. Since the early-time characteristics of the radiation field in all the experiments are similar, it is unsurprising that (at early times) all three front trajectories are also similar.

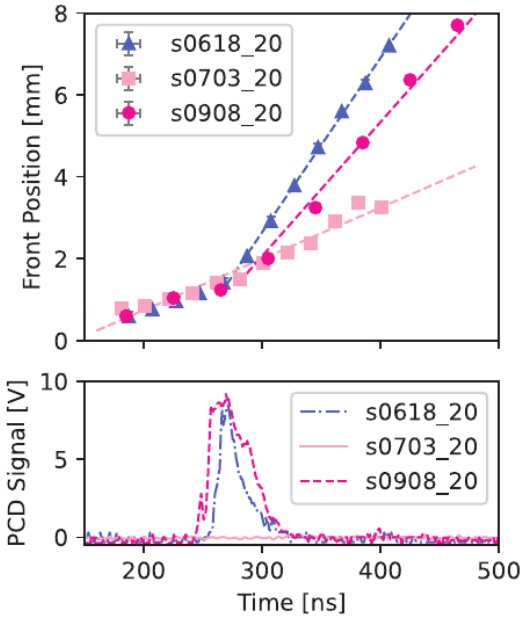

*Fig. 7 Top - Position of ablation front measured from optical self emission imaged, captured with a fast-framing camera in three separate experiments. Bottom - Signal from a PCD, filtered with 20 um of Beryllium foil ($\epsilon_\gamma \gtrsim 700$ eV), and capturing emission from the Z-Pinch in the same three experiments*

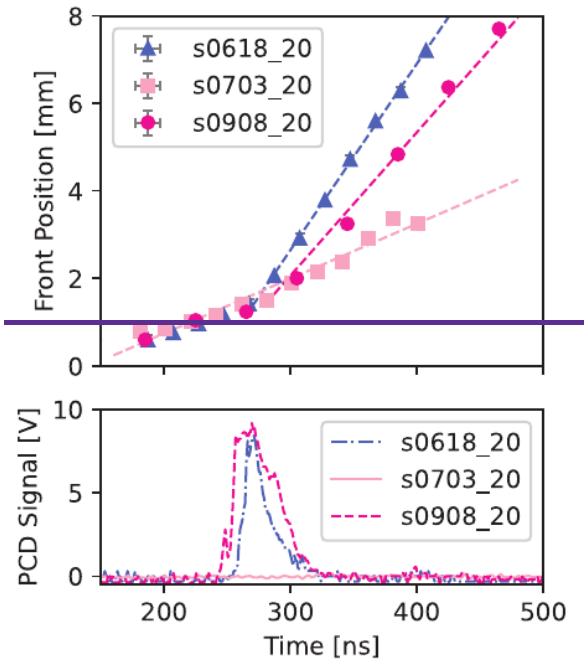

In an attempt to provide more quantitative data on the plasma ablating from the target Thomson scattering was employed. This diagnostic provided measurements of temperature and bulk velocity, from several spatially localized scattering volumes. The Z position of the probing laser was set so it passed just above the silicon target. This was done to allow the laser pulse to exit the experimental volume, rather than dumping its energy into the target and perturbing the plasma conditions.

Fig. 8 shows the position of Thomson scattering volumes, and flow velocities inferred from best fits to scattering spectra obtained for each of these volumes. The profile for plasma velocity monotonically increases with position from the target, starting at around 1×10^6 cm/s, and increasing up to a maximum of 4×10^6 cm/s. The front velocity, measured from self-emission images, was 3.3×10^6 cm/s . The plasma velocity measurements obtained with Thomson scattering are broadly speaking consistent with this value, considering our earlier comment that it is unclear what point in the density profile corresponds to the front position in self emission.

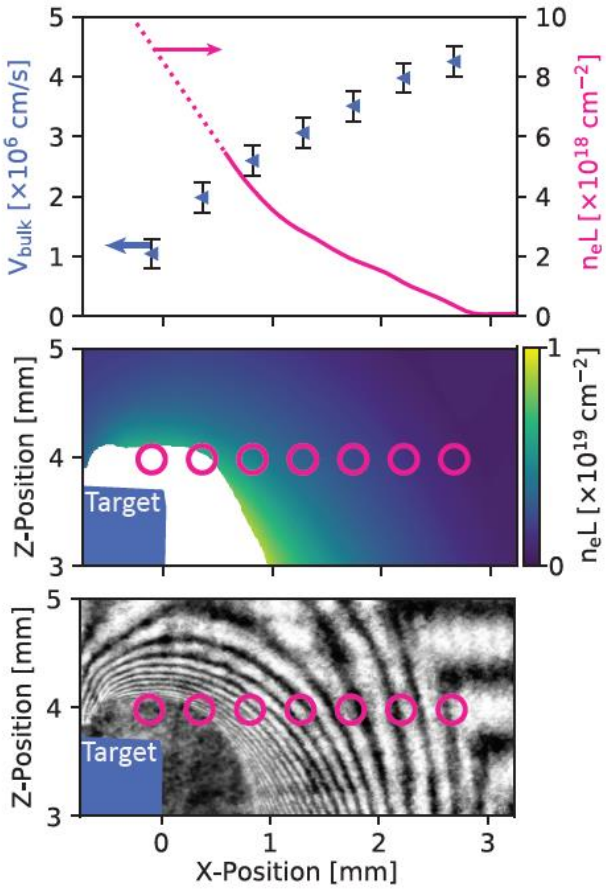


*Fig. 8 Thomson scattering data for eight (spatially separated) scattering volumes, obtained 295 ns after current start. (**Top**) Measured plasma velocity, and line integrated electron density (obtained with interferometry). (**Middle/bottom**) Position and size of the scattering volumes overlaid on an electron density map / interferogram from the same experiment.*

***Plasma temperature and ionization – the limits of Thomson scattering***

The conditions of the X-Ray ablated plasma are significantly colder and denser than we have encountered in previous Thomson scattering experiments on MAGPIE. Whilst this does not appear to reduce the accuracy of the measured velocity profile, which was presented above, it

does significantly affect measurements of plasma temperature. Two factors compound to make temperature measurements more challenging than would usually be the case:

1) The Thomson probe significantly heats the plasma flow via inverse Bremsstrahlung
2) The effect of ion-ion collisions alters the ion-acoustic response of the plasma (which is what is probed with the MAGPIE Thomson scattering diagnostic).

The effect of heating was something which we treated through radiation hydrodynamics modeling, and which is discussed in section 4. The effect of ion-ion collisions has been discussed in a series of publications by Rozmus et. al[9]. In collaboration with this group we have made some progress in treating the effect of collisions on the Thomson spectra measured in these experiments. We have focused our attention on the scattering volume at X = 2mm, as the simulations we have performed suggest that this volume is largely unaffected by probe heating.

For this volume, we find that the ion and electron temperatures are equilibrated at a value of around 13 eV, and the average degree of ionization is around 7. It is interesting to note that a collisional-radiative atomic model predicts an average charge state closer to 4 for these conditions. A possible explanation is that re-radiation from the target has some influence on the charge state distribution in the ablated plasma flow.

***Magnetic field measurements***

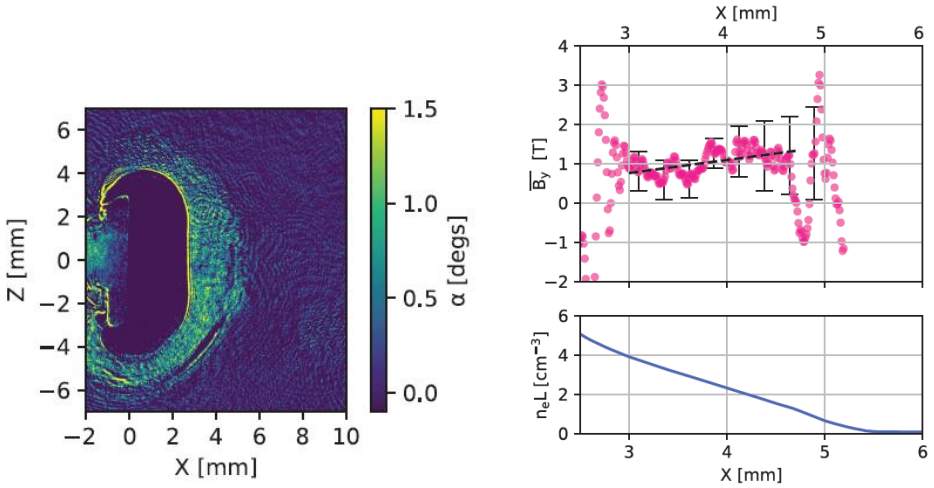


*Figure 9* ***(Left) S****patially resolved values of rotation angle, obtained with a laser polarimetry diagnostic. (****Right****) Values of (weighted average) magnetic field strength as a function of position.*

As mentioned previously, the silicon plasma expands into a magnetic field ~ 10 T, which is supported by current flowing through the Z-Pinch. To assess the penetration of this field into the plasma, Faraday rotation imaging data was captured in a separate experiment, also with a separation of 40 mm between the pinch and the target. The diagnostic measures a weighted average of the component of magnetic field parallel to the path of the probing laser. The weighting is given by

$$\langle B_y \rangle = \frac{\int n_e(\boldsymbol{r})\, \boldsymbol{B}(\boldsymbol{r}) \cdot d\boldsymbol{y}}{\int n_e(\mathbf{r}) d\boldsymbol{y}},$$

where the line integral runs along the path of the probing laser. To apply Faraday rotation to X-Ray ablated plasma flows we had to adjust the diagnostic to account for significant laser probe absorption by the plasma.

Fig. 9 shows a profile $\langle B_y \rangle$, along the line Z = 0 mm, plotted along with the profile of $n_e L$ from interferometry. The field profile includes some sharp oscillations at around 2.7 mm and 5 mm from the target. These features are non-physical and originate from caustics in the experimental data. The signal in the region bounded by these caustics is reliable, and indicates a relatively flat profile of average magnetic field with an average value of 1 T. This is significantly smaller than the field in the vacuum, which is closer to 10 T at this time, suggesting that the field is largely frozen out of the plasma.

To support the measured field profile, the system would have to drive current in a thin layer at the interface between the plasma and the vacuum. Although the current profile imposed by an external voltage source might have a different profile, this result is still significant: It places a constraint on resistivity at the plasma vacuum interface. In the future this could help in the development of a model for solar-cell disruption in response to a prompt X-Ray burst.

## 3.2 'Low Flux' Experiments

Initial low flux experiments were carried out again using simple planar silicon targets, but with a target to pinch distance increased to between 40 cm and 150 cm. The plasma conditions were diagnosed using a fast-framing camera, and differentially filtered optical diodes which were aligned to collect self-emission from the target plasma. The target assembly is shown below in Fig. 10 (a).

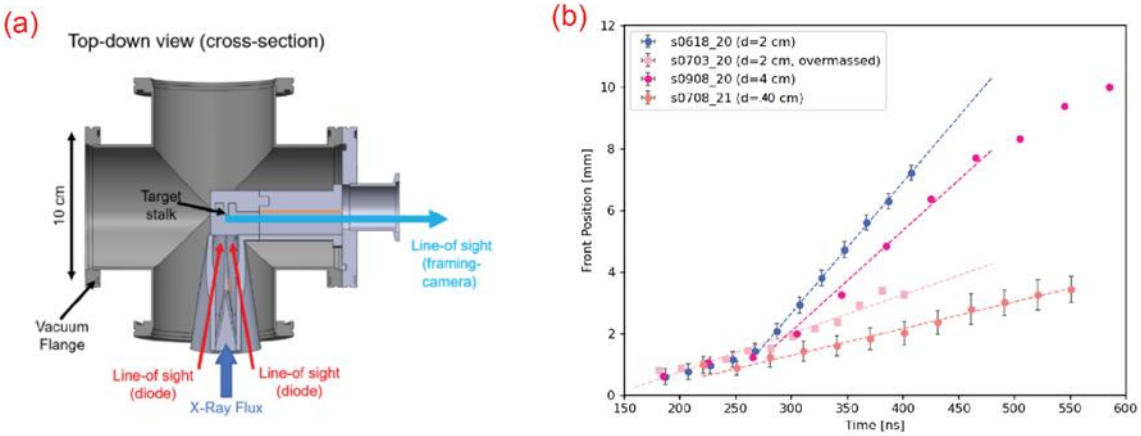


*Fig. 10 – (a) Target assembly for initial low-flux experiments, showing the position of optical diodes and the line of sight for the framing camera; (b) Front position as a function of time in high and low fluence experiments.*

The diodes unfortunately returned no meaningful data, as the optical self-emission from the silicon plasma was overwhelmed by reflected light from the Z-Pinch. The fast-framing camera recorded self-emission from the silicon plasma at a target distance of 40 cm (fluence on-target ~ 1 J/cm$^2$), but not at 1m or beyond (fluence ~0.15 J/cm$^2$). The absence of a recorded signal in self emission at target separations greater than 40 cm suggested that the densities of the plasmas produced under these fluences were too low to be reliably measured with self-emission imaging or laser probing diagnostics. To try and diagnose the conditions of these plasmas, we have begun experiments utilizing biased electrical probes, attached to, or placed close to the silicon targets. Fig. 11 shows a photograph and diagram of this experimental setup. As can be seen in the figure, two probes were placed near to the silicon. Each was separately biased, with the voltage relayed to the probe via a coaxial line. The two probes were biased to $\pm 10$ V respectively.

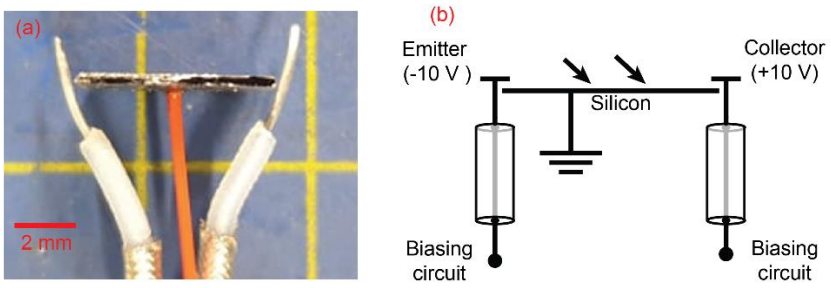


*Fig. 11 – (a) a setup photograph of an experiment where two biased probes were placed in the vicinity of the silicon target; (b) a diagram of the same experimental setup – the biasing circuit is shown in figure 12.*

The circuit used to maintain the bias voltage on one of the two probes is shown below. In this circuit, the 30 nF capacitor provided the bias voltage on the experimental timescale and also acts as a high-pass filter for a signal which is relayed to an oscilloscope via a coaxial line. This bias/monitoring configurations is commonly used for X-Ray flux measurements in pulsed-power driven experiments [Chandler 1999].

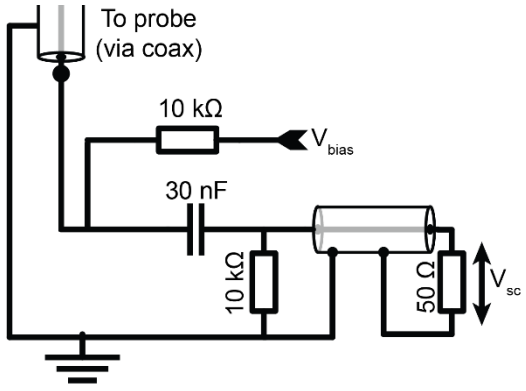


*Fig. 12 – Diagram of the biasing circuit used for low flux experiments with silicon.*

Fig. 13 shows the signal obtained from the positive and negatively biased probes as a function of time; the signal from a pair of photo-conducting diamond (PCD) X-Ray detectors; and the signal from a Rogowski coil, which measures the time-derivative of current through the Z-Pinch. The spectral filtering of the two PCDs was provided by Mylar and aluminum foils. The mylar filtered detector is sensitive to the soft X-rays from the precursor plasma. The Aluminum filtered detector is sensitive only to X-Rays emitted in the main implosion.

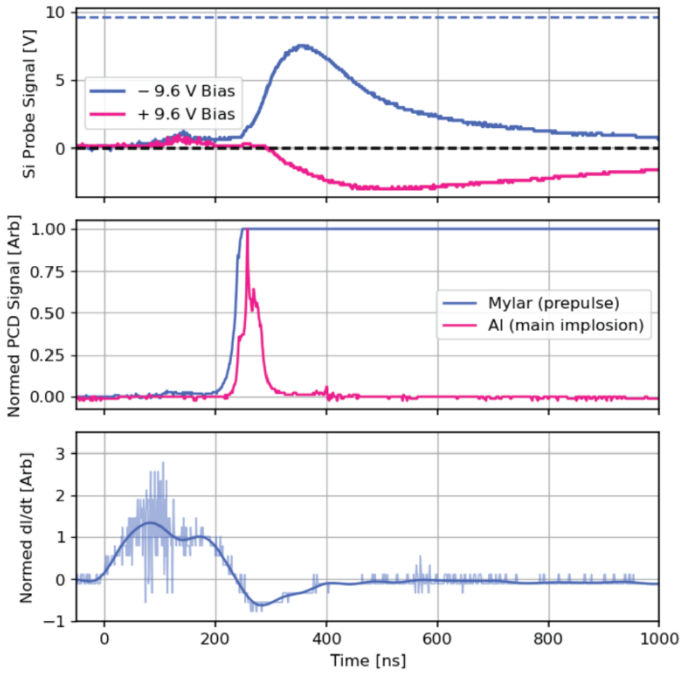


*Fig. 13 – (top) voltage measured on the 2 biased probes; (middle) X-Ray signal on filtered photo-conducting diamond (PCD) detectors; (bottom) time-derivative of current through the pinch as measured by a Rogowski coil.*

The data in the figure shows that the voltage on the probes remains approximately constant at the time when current first flows through the pinch. This is encouraging in the sense it demonstrates the probes are well shielded from the electromagnetic noise produced by the generator. At a time which coincides with the arrival of pre-pulse X-Rays, a change in the voltage on the negatively biased probe is registered. This signal increases significantly when the X-Rays from the main implosion begin to irradiate the target. The onset of a signal on the positively biased probe is delayed by approximately 30 ns, and the signal is of a lower amplitude than that seen on the negatively biased probe. A potential explanation for the asymmetry between the two probes could be the emission of photoelectrons from the negatively biased electrode. It is possible that these electrons could play a role in initiating subsequent arcing.

A key point to take away from the data in this plot is that the bias on the two probes continues to change for many hundreds of nanoseconds after the X-Rays from the Z-Pinch are switched off – indicating the presence of a plasma on the surface of the silicon for this time period, and the formation of a current carrying channel which connected the two probes within the silicon plasma

## 4.0 SIMULATIONS AND THEORETICAL MODELLING

### 4.1 Modelling of High Flux Experiments using Chimera

The radiation magnetohydrodynamics code Chimera[10] was used to perform simulations for the high flux experiments detailed in Section 3.1. 2D simulations investigated the ablated plasma dynamics and effect of magnetic field on the ablation. Detailed 3D simulations of the imploding wire array were performed to characterize the X-ray drive and provide frequency dependent drive spectra for the ablation simulations.

Fig. 14 shows the mass density at peak X-ray emission for a 3D Chimera simulation for a 32 x 13μm aluminum wire array with the MAGPIE current drive applied. Perturbations are introduced to the expanded wire cores to seed instabilities in the implosion. This is necessary to match the timing and intensity of X-ray production as well as the morphology of the stagnated pinch - similar structure is visible in Fig. 2.

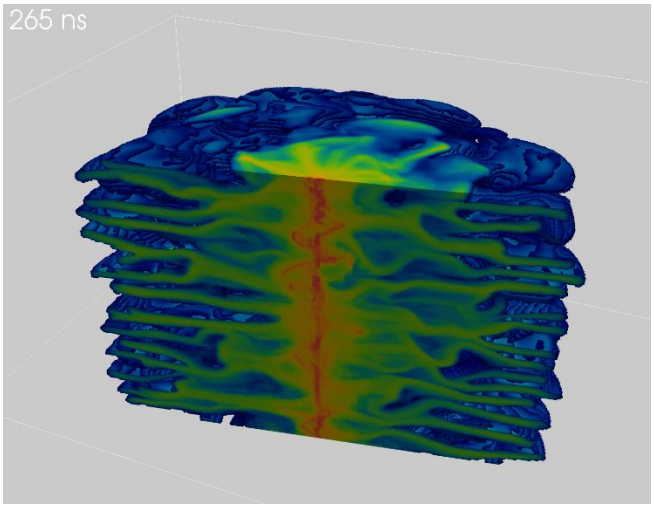


*Fig. 14: 3D colour plot of the mass density at peak X-ray emission in a 3D Chimera simulation for the experimental Al wire array set up.*

The X-rays produced by the pinch include bremsstrahlung, recombination and spectral line emission. The atomic physics code SpK was used to calculate the spectrally resolved opacities used in both inline and post-process calculations of the emitted X-rays. Fig. 15 shows the X-ray power time history and time-integrated spectrum from the 3D Chimera simulation. The presence of significant precursor emission as well as the fast rise, slow fall and FWHM of the stagnation pulse line up with experimental observations. The time-integrated spectrum shows K-shell emission lines as well as continuum at high energies, from bremsstrahlung and recombination, and low energies, from broadened and merged L-shell emission lines.

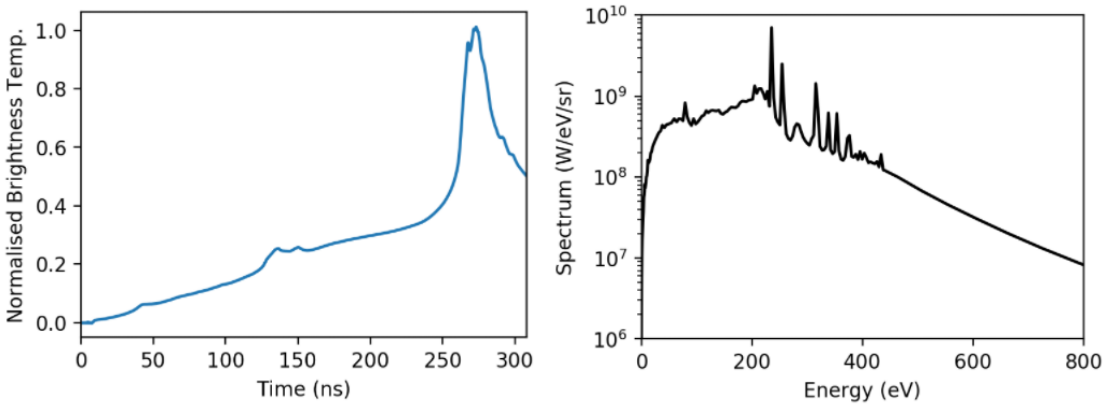


*Fig. 15: (Left) Normalised brightness temperature emitted from 3D Al wire array simulation giving a total released X-ray energy of 15 kJ. (Right) Time integrated spectrum calculated from radiation transport post-processing of the Chimera simulation.*

For the Si ablation simulations, idealized radiation and magnetic field sources were used to drive a x-z simulation with magnetic field along y – see Fig. 16. The radiation intensity was scaled down until expansion matched experimental measurements, this corresponded to a peak brightness temperature on target of approximately 10 eV. By comparison to interferometry data, it was found that the presence of the magnetic field from the Z-pinch tamped the expansion of the ablated plasma. The plasma and magnetic pressure relaxed such that the edge of the expanded plasma was close to isobaric with the vacuum magnetic field, preventing instability growth. The simulated magnetic field diffuses into the plasma and the corresponding surface current leads to Ohmic heating of the edge plasma. These results are summarized in Fig.17.

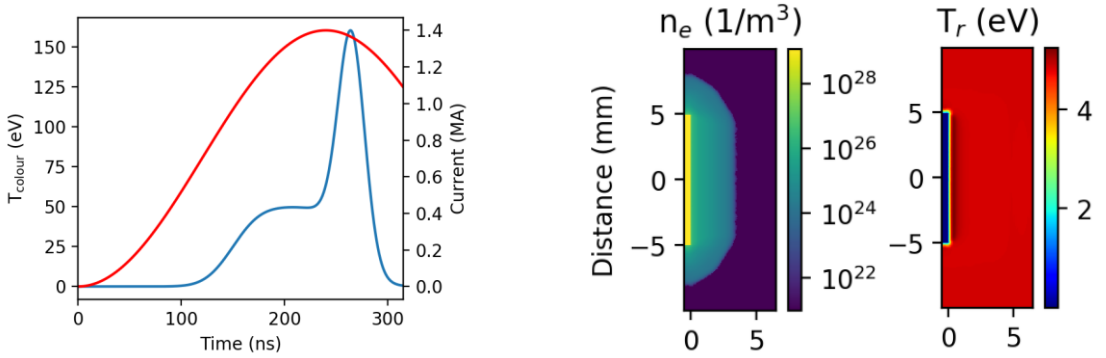


*Fig. 16: (Left) Radiation drive (in blue) and current time history used to source magnetic field (in red) in 2D Si ablation simulations. (Right) Contour plots showing simulated electron density and radiation temperature 30 ns after peak X-ray drive.*

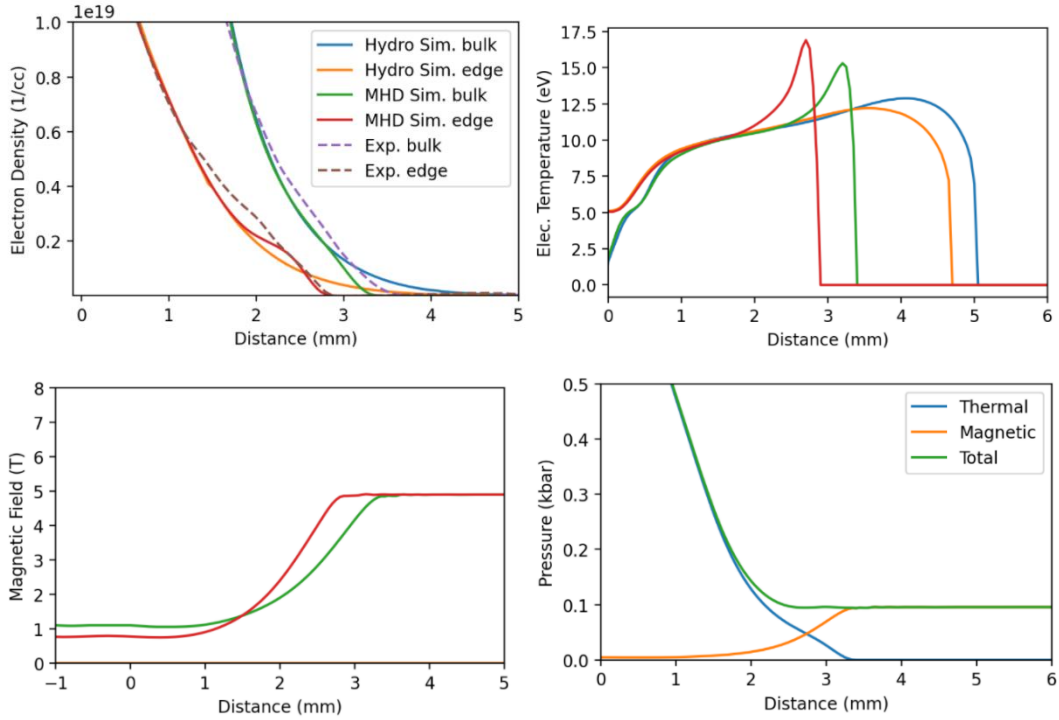


*Fig. 17: Lineouts from HD (B=0) and MHD simulations, the bulk lineout was taken through the centre of the target and the edge lineout 0.5mm above the target edge. (Top left) Electron density with experimental interferometry results in dashed lines, (top right) electron temperature, (bottom left) magnetic field. (Bottom right) The thermal and magnetic pressure lineouts from the MHD simulation showing near pressure balance at the plasma edge.*

In general, the overall morphology of the ablation flow, density profile, temperatures, and velocity profiles which we obtain in the simulation are in excellent agreement with experimental data. The one area where there is a significant discrepancy between the experiment and the simulation is in the profile of magnetic field. Here the simulation predicts a profile which is more diffusive than the one seen in the experiment. The reason for the disagreement is still unclear, and in future are planning to obtain additional experimental data to measure the current profile at the plasma vacuum interface.

***Modeling of Thomson probe heating***

As discussed in Section 3.1, there was a need to explore the possibility of Thomson probe heating via inverse Bremsstrahlung. To study this effect, we exploited the laser heating capability in Chimera. Below a temperature map from a simulation in which the Thomson probe included. The results show that the heating is significant for much of the outflow, however the least dense region of the outflow is largely unaffected. For this reason, we restricted the experimental temperature measurements we report to this region of the outflow.

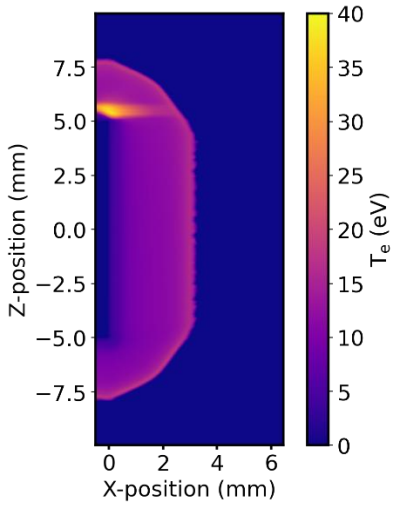


*Fig. 18: A heatmap of Temperature in a silicon ablation simulation, showing plasma heating by the Thomson probe laser.*

## 4.2 A simple theoretical model of the energy deposition process in high flux experiments

In high flux environments, such as those discussed in Section 3.1, the target mass is rapidly heated to a plasma state and ablated. The sub-sonic Marshak wave which drives the ablation process is best described using radiative-hydrodynamics codes. However, in low fluence environments the energy deposited in the material is comparable to the latent heat of phase changes. Therefore, simulation of this process requires a different set of models. The goal of these simulation tools is to understand the energy deposition processes which lead to plasma formation on the solar panel surface.

First, we must consider the transport of the incoming radiation into a static solid target. This is dominated by absorption as the material temperatures are low. One can compute the radiative heating rate using the material's cold opacity as follows:

$$Q_{rad}(x) = \int I_{inc}(h\nu)\ \kappa_c(h\nu) e^{-\kappa_c(h\nu)\ x}\ dh\nu$$

The heating rate is maximal at the target surface (x=0) and if one assumes the incoming radiation is a blackbody then the surface heating rate can be expressed in terms of the Planck opacity:

$$\text{Max}(Q_{rad}) = I_0\ \kappa_p(T_r)$$

In the absence of thermal conduction, if the radiative heat delivered to the surface exceeds the latent heat, then a phase change will occur. This allows us to define a threshold fluence, above which we expect dynamics to play a role as the target ceases having a solid surface. For example, the threshold fluence for vaporisation is given by:

$$F_v^{\text{vap}} = \frac{H^{\text{vap}}\rho}{\kappa_p(T_r)}$$

Where $H^{\text{vap}}$ is the specific heat of vaporisation and $\rho$ is the solid mass density. In the presence of thermal conduction, the time scale over which this radiation is deposited becomes important. If the radiative flux is low then the heat deposited can be conducted away from the surface, preventing melt and vaporisation. Solving the heat equation semi-analytically gives the energy density as a function of depth into the target:

$$U(x,t) = \int_0^t \int_0^\infty \frac{1}{\sqrt{4\pi k(t-t')}} \left( \exp\left( -\frac{(x-x')^2}{4D(t-t')} \right) + \exp\left( -\frac{(x+x')^2}{4D(t-t')} \right) \right) Q_{rad}(x',t')dx'dt'$$

Where D is the thermal diffusivity which is assumed constant. Solving this equation for specified material properties and incoming radiation pulse allows a more complete picture of the energy deposition profile in the target. It can be shown that the surface energy density is approximately given by:

$$U(x=0,t) \approx \kappa_p \int_0^t I(t') e^{\frac{t-t'}{\tau}} \left( 1 - \text{erf}\left[ \sqrt{\frac{t-t'}{\tau}} \right] \right) dt', \qquad \tau = \frac{1}{D\kappa_p^2}$$

Where I(t) is the spectrally-integrated pulse intensity as a function of time. If we assume a uniform drive of length $\Delta t$, then the energy density at the surface at the end of the drive is:

$$U(x=0,\Delta t) \approx I_0 \kappa_p \cdot f\left(\frac{\Delta t}{\tau}\right), \qquad f(x) = \frac{1}{x} \cdot \left( e^x \left( 1 - \text{erf}\left(\sqrt{x}\right) \right) - 1 + \sqrt{\frac{4x}{\pi}} \right)$$

Where f(x) is a monotonically decreasing function (and f(0) = 1). Finally, considering the energy density required for vaporisation links back to the threshold fluence but now with the effects of thermal conduction included:

$$F_{v,th}^{\text{vap}} = \frac{H^{\text{vap}}\rho}{\kappa_p(T_r) f\left(\frac{\Delta t}{\tau}\right)} = \frac{F_v^{\text{vap}}}{f\left(\frac{\Delta t}{\tau}\right)}$$

This simple model allows us to approximately predict the radiative fluence at which the target surface will undergo a phase change. The ideal material to resist surface phase change would have high latent heat, low opacity and high thermal diffusivity - a rather intuitive result. Fig. 19 shows the pure radiative threshold fluence and radiative-thermal threshold fluence for some common satellite materials to cause vaporisation.

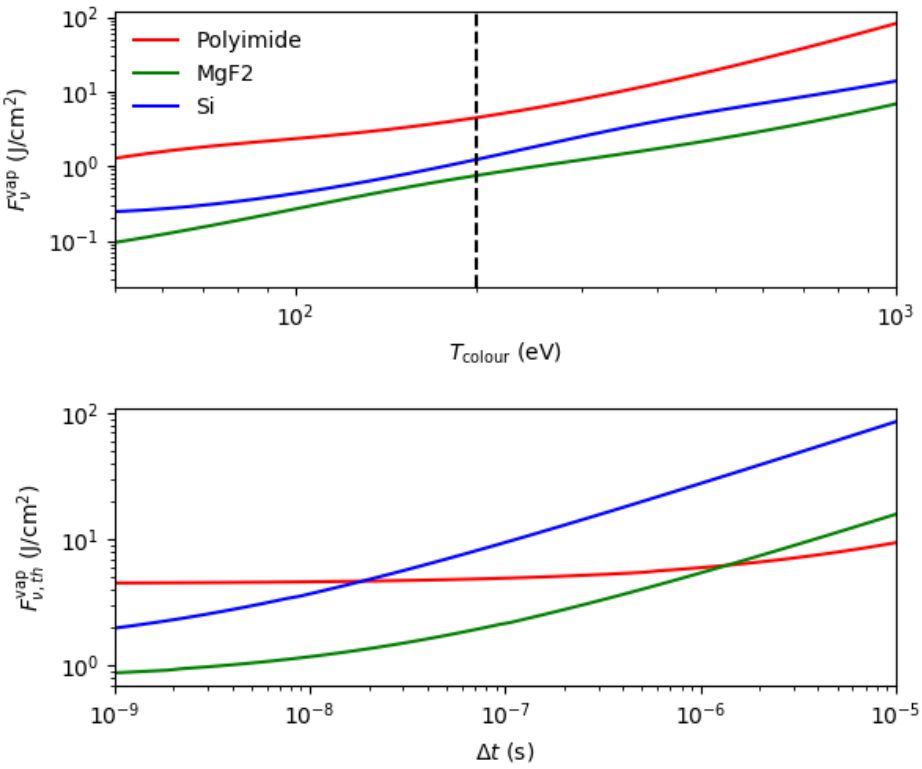


*Fig. 19 – (Top) Radiative threshold fluence as a function of incident blackbody colour temperature. (Bottom) Threshold fluence including the effects of thermal conduction within the target as a function of drive duration. These have been plotted for a colour temperature of 200 eV.*

It is found that the typical vaporization threshold fluences are in the 1-10 J/cm$^2$ range (at the upper limit of the low flux experiments reported in Section 3.2). It should be noted that the latent heat of fusion is typically 3 orders of magnitude below that of vaporization. Therefore, one can expect 1-10 mJ/cm$^2$ fluences to begin melt on the target surface. The above model predictions used fixed, room-temperature values of thermodynamic properties. The evolution of these properties during heating would affect the final result but the pure radiative threshold fluence will still remain the lower limit. One can also solve the heat equation numerically to get a more complete picture of the heating profile in the target. Fig. 20 shows a solution for a 200 eV blackbody drive which has a 20ns FWHM Gaussian drive profile and an on-target fluence of 5 J/cm$^2$. In the absence of thermal conduction, we see this would be sufficient to vaporize $MgF_2$ and Si. However, the high thermal diffusivity of Si increases its threshold fluence for tens of nanosecond drives. This leads to a flat energy density profile into ≈ 1 micron of the target.

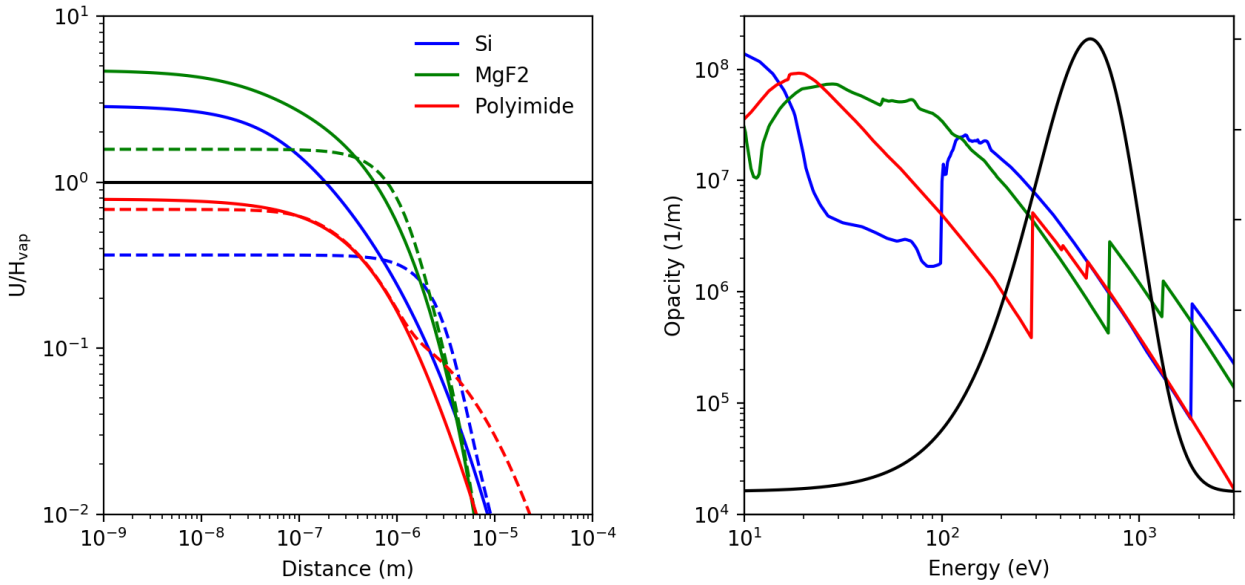


*Fig. 20 – (Left) Normalised energy density as a function of position into target for various materials after a 5 J/cm$^2$ incident radiative fluence with 200 eV blackbody spectrum and 20 ns FWHM. Solid lines are the profiles in the absence of thermal conduction while the dashed lines include thermal conduction. (Right) Cold opacities as a function of photon energy taken from Henke. The black line shows a 200 eV blackbody spectrum for reference.*

Another assumption of the above models is the use of a blackbody spectrum for the incident radiation. While this is a suitable parameterization of the spectrum – and more relevant to that expected from a nuclear detonation - the MAGPIE Z-pinch X-ray source used to provide initial quantitative comparisons will also contain Al L- and K-shell lines. The exact form of the incident spectrum will alter the threshold fluence, but we expect this to be a higher order effect on the threshold for phase change.

## 4.3 A Theoretical Model for the Behavior of Photo-electrons

As suggested in Section 4.2, a soft X-ray flux at 1-10 J/cm$^2$ could be expected to vaporize the surface of typical solar cell materials, but much higher fluences would still required to form a conductive plasma. Therefore, we turn to investigate how the photo-electrons produced by the X-ray fluence behave – this would be the likely be the initiator of damage in lower flux environments, representing the effects at large distances from a nuclear detonation. Accurate modelling of the photo-electrons is complex as they can collide and thermalize with the material or escape the material surface. A ballpark estimate of the number density of photo-electrons produced can be found from the opacity (assuming it is dominated by the photo-ionization cross sections) and incident photon number flux. For 100 mJ/cm$^2$ incident radiation with a 200 eV blackbody spectrum on Si, a photo-electron number of density of is 6 x $10^{19}$ cm$^{-3}$ is found, which is 0.01 % of the total (conduction and valence) electron number density. This requires a new theoretical model of the photo-electron production, transport and thermalization processes, also including the effect of any bias voltage provided by the solar cells.

The bias voltage across the cells can act as an accelerating field on these photo-electrons. Therefore, they will accelerate up to higher energies as they travel towards an anode. In their transit they can undergo a number of collisional processes. We assume this photo-electron population to be a minority and will be interacting with a neutral background gas. This electron population can elastically scatter or cause collisional ionization and excitation. We are interested in whether a minority population under the presence of an electric field can cause a cascade and resulting breakdown of the gas.

One existing relation to consider is Paschen's law, which gives the breakdown voltage as a function of pressure-anode cathode (AK) gap product. The Paschen curves typically exhibit a minimum breakdown voltage in 100s of volts around 0.01-0.1 atm-mm. However, experiments on MAGPIE in the low flux regime described in Section 3.2 used bias voltages of approximately 20 V – likely below the breakdown voltage for any forming Si vapour. These experiments saw a sustained current carrying channel after the photo-electrons source had ended operating below the breakdown voltage. Therefore, it seems that a mechanism different from the canonical Paschen breakdown is occurring. To study the behavior of the photo-electrons, we consider a zero dimensional electron Boltzmann equation with an externally applied electric field:

$$\left[\frac{\partial}{\partial t} - \frac{e}{m_e}\underline{E}\cdot\nabla_v + n_t\sigma_t v\right] f_e = n_t S + n_t R_e + n_t R_{c.e.} + n_t R_{c.i.}$$

Where $f_e$ is the electron distribution function (EDF), $n_t$ is the number density of target atoms (i.e. neutral gas density), $\sigma_t$ is the total interaction cross section, $S$ is the photo-ionization rate per unit number density and the $R$'s give the collision operators for various interactions between electrons and neutral gas atoms.

A moment analysis of this equation can be done to determine some behaviors of the electron population. For example, taking the zeroth moment allows us to find the rate of change of fractional electron density:

$$\frac{\partial}{\partial t}\left(\frac{n_e}{n_t}\right) = S(t) + \int \left(Y_m\sigma_m - \sigma_a\right) v^3 f_0(v) dv$$

Where $f_0$ is the isotropic EDF, $\sigma_a$ is the cross section from absorption processes, $\sigma_m$ is the cross section from multiplying processes (e.g. collisional ionization) and $Y_m$ is the yield of those multiplying processes. The multiplying process will have an energy threshold, and thus for the gas to be a multiplying medium for electrons, the electron population must be sufficiently energetic such that the integral can become positively valued. For reference, the first ionization energy of silicon is 8.15 eV and therefore an electron accelerated from zero in the applied 20V bias field could not reach this required energy in the < 10mm AK gap. Therefore, it is only the photo-electron population from the X-ray fluence that multiply in the medium.

With the first moment, we can evaluate whether a stable electron drift is set up or a run-away is started. This is similar to the calculation of Dreicer on the electric field required to produce runaway electrons in a collisional plasma. With some manipulation, the drift equation can be written as:

$$\frac{\partial V_e}{\partial t} = \frac{eE}{m_e}(\varphi(V_e) - 1)$$

Where $V_e$ is the average electron drift and $\varphi(V_e)$ is a collisional drag term which exact form isn't needed in the following. Importantly, a runaway drift will occur if the maximum value of $\varphi(V_e) < 1$. We can consider a phenomenological argument for the critical field when a run-away will occur. If we consider the electrons will have a most probable speed of $\sqrt{2kT/m_e}$, then the time between collisions is given by $\tau$ and for these electrons to double in speed between collisions then accelerating field must be given by:

$$\tau = \frac{1}{n_t \sigma \sqrt{2kT/m_e}}, E_c = \frac{m_e}{e}\frac{\sqrt{2kT/m_e}}{\tau} = \frac{2}{e} kT\, n_t \sigma(kT)$$

As expected, the critical field scales with neutral density. Typically, cross sections are a decreasing function of energy and therefore it is easier to produce drifts with hotter initial electron temperatures as they have longer mean free paths. As discussed in Dreicer, operating at electric fields below the critical field induce more collisional heating as the run-away electrons do not couple energy back to the medium.

To study the electron kinetics more quantitatively, we construct a numerical model of the 0D electron Boltzmann equation. Due to its structure, it resembles a transport problem in 1D spherical geometry but in 1D spherical velocity space where the direction of the electric field sets the effective radial coordinate. In a conservative form:

$$\frac{\partial f_e}{\partial t} - \frac{eE}{m_e}\left(\frac{\mu}{v^2}\frac{\partial}{\partial v}(v^2 f_e) + \frac{1}{v}\frac{\partial}{\partial \mu}\left((1-\mu^2) f_e\right)\right) = -n_t \sigma_t v + n_t S + n_t R_e + n_t R_{c.e.} + n_t R_{c.i.}$$

Thus, we use time-dependent discrete ordinates methods to discretize the equation into velocity magnitude, $v$, cosine of the electron velocity angle with respect to the electric field, $\mu$, and time, $t$. We also note that normalizing $f_e$ by $n_t$ removes all number density dependence, i.e. we consider an EDF *per* neutral atom. The Legendre-Gauss quadrature set was used for the angular ordinates, $\mu$, and the canonical conservative angular differencing coefficients were used.

For $\mu_n > 0$

$$\left(\frac{\mu}{v^2}\frac{\partial}{\partial v}(v^2 f_e) + \frac{1}{v}\frac{\partial}{\partial \mu}\left((1-\mu^2) f_e\right)\right)$$
$$\rightarrow \frac{\mu_n}{V_i}\left[\left(A_{i+1/2} + A_{i-1/2}\right) f_{n,i-1/2} - 2A_{i-1/2} f_{n,i}\right]$$
$$+ \frac{A_{i+1/2} - A_{i-1/2}}{V_i w_n}\left[2\alpha_{n+1/2} f_{n,i} - 2\left(\alpha_{n+1/2} + \alpha_{n-1/2}\right) f_{n-1/2,i}\right]$$

For $\mu_n < 0$

$$\left(\frac{\mu}{v^2}\frac{\partial}{\partial v}(v^2 f_e) + \frac{1}{v}\frac{\partial}{\partial \mu}\left((1-\mu^2)f_e\right)\right)$$
$$\rightarrow \frac{\mu_n}{V_i}\left[-\left(A_{i+1/2} + A_{i-1/2}\right)f_{n,i+1/2} + 2A_{i+1/2}f_{n,i}\right]$$
$$+ \frac{A_{i+1/2} - A_{i-1/2}}{V_i w_n}\left[2\alpha_{n+1/2}f_{n,i} - 2\left(\alpha_{n+1/2} + \alpha_{n-1/2}\right)f_{n-1/2,i}\right]$$

Where $w_n$ are the quadrature weights, $A_{i+1/2}$ is the velocity space area and $V_i$ is the velocity space volume. These equations can be directly compared to spatial analogues such as in Lewis and Miller, Computational Methods of Neutron Transport.

The time-stepping was performed using the fictious source method. The collision and transport operators are evaluated implicitly, leading to the following linear system:

$$\left[\boldsymbol{L} + \boldsymbol{C} + \frac{1}{\Delta t}\mathbf{1}\right] f_e^{i+1} = \frac{1}{\Delta t} f_e^i + \frac{1}{2} n_t\left(S(t) + S(t+\Delta t)\right), \text{equivalent to } \boldsymbol{A}x = b$$

Where $\boldsymbol{L}$ is the transport operator, $\boldsymbol{C}$ is the collision operator and $\mathbf{1}$ is the identity matrix. The linear algebra solve is performed using the LAPACK routines wrapped by python numpy.

This gives a model, which even with a simple collision operator, can show relevant electron dynamics. For example, we can consider the effect of a 4 kV/m (20 V over 5mm as in Section 3.2) applied electric field on a burst of initially 10 eV photo-electrons over 200 ns time-scale. The numerical model using 16 angular ordinates, 128 velocity cells up to a maximum energy of 800 eV. Fig. 21 below compares their evolution for two different elastic scattering cross sections (form motivated by Lagushenko and Maya):

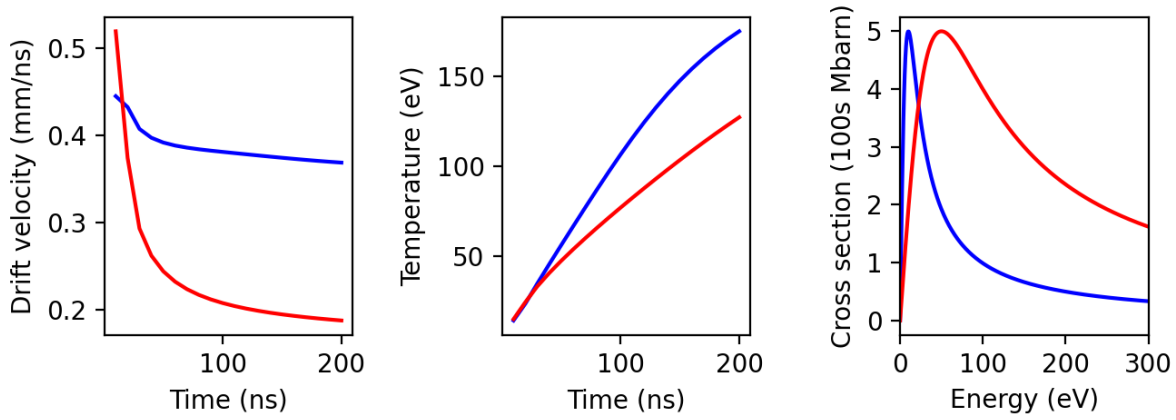


*Fig. 21 Properties of initially 10eV photoelectrons produced by soft X-ray burst with a 4kV/m applied electric field and different scattering cross sections*

As seen, the electrons can get Ohmically heated to high temperatures in realistic applied fields. Thus, we can expect collision ionization to take place and increase the electron population.

With further development and a more complete collision operator, this model is capable of predicting the cascade dynamics as a function of bias field, $E$, and photo-electron source, $S$, in the low electron density regime. Initial attempts were taken at implementation of the Lotz collision ionization cross section, Lagushenko and Maya elastic and collisional excitation cross sections and the Clark differential cross section for ionization[11]. In addition, a more realistic photo-electron source term is needed and a loss term for when electrons impact the cathode. Further testing and validation are required before these can be used to form X-ray driven cascade predictive models.

## 5.0 SUMMARY

We have successfully created a pulsed power platform for exploring the effects of prompt soft X-rays on solar panel materials. We have performed multiple experiments with Silicon (and plastic) targets in a high flux regime with deposited energies up to ~ 400J/cm$^2$ and intensities ~10GW/cm$^2$; and have made initial experiments at much lower fluxes. Obvious ablation was seen from the front of Silicon targets with high fluxes, as we moved to experiments with energies <1J/cm$^2$ and intensities 25MW/cm$^2$ ablation was no longer observed, however biased pick-up probes across the Silicon target recorded a current, which was initiated at the same time as soft X-ray emission and continued for many 100s of ns after this ended. This and asymmetries in the signals between differentially biased probes suggested that photo-electron emission was responsible for the increase in conduction at the surface of the target.

Experimental results led to significant improvements in the atomic modelling packages of the Chimera RMHD code, which was then able to accurately simulate the ablation of plasmas in high flux experiments and explore the effects of magnetic field on this ablating plasma. Simple theoretical models were developed to explore how the ablation of target materials varied with the intensity of incident soft X-rays. For lower flux experiments, a new model of electron behavior highlighted that even with relatively small applied electric fields (of the same order that might be found in solar panels), emitted photo-electrons could be heated to relatively high temperatures enabling collisional excitation with surrounding material, an increase in population and hence a rise in conduction (which could be the basis of arcing).

## 5.1 Future Research into Soft X-ray Effects on Solar Panel Materials

Whilst we were able to perform multiple experiments in the high flux regime with targets relatively close to the X-ray source; disappointingly our experimental work at much lower fluxes was significantly affected by equipment problems, both with the pulsed power facility itself and in the diagnostics we were attempting to utilize to make measurements at other facilities. These were compounded by the Covid pandemic resulting in multiple ‘lockdowns’, a lack of personnel and supply chain issues.

It is clear that further experiments at relatively low X-ray fluxes would enable further improvements to our modelling of the behavior of solar panels in a regime of interest to DTRA and its sponsors, and represents an interesting area of physics for us to explore academically. With the recent repair of the MAGPIE facility and its improved operation, we are looking to continue this research in undergraduate student projects over the next 1-2 years (at no cost to DTRA). This will build on significant preparation work already carried out by researchers which is detailed below, and we will provide the results to DTRA as they become available.

**Design of new low flux experiments with biased Kapton targets**

To investigate the behavior of X-Ray driven plasma arcs in Kapton, we have developed the target shown in Fig. 22. This consists of Kapton tape on a 3D printed plastic substrate. The Kapton is

bounded on 2 sides by copper electrodes. The other 2 sides of the Kapton are open for diagnostic access and the front surfaces of the copper electrodes are covered with Kapton to exclude the direct X-Ray irradiation of the metal.

The area of Kapton bounded by the electrodes was ~ 1 $cm^2$. The electric field on the surface was designed to be comparable with that expected within solar cells, to facilitate extrapolation between the two systems.

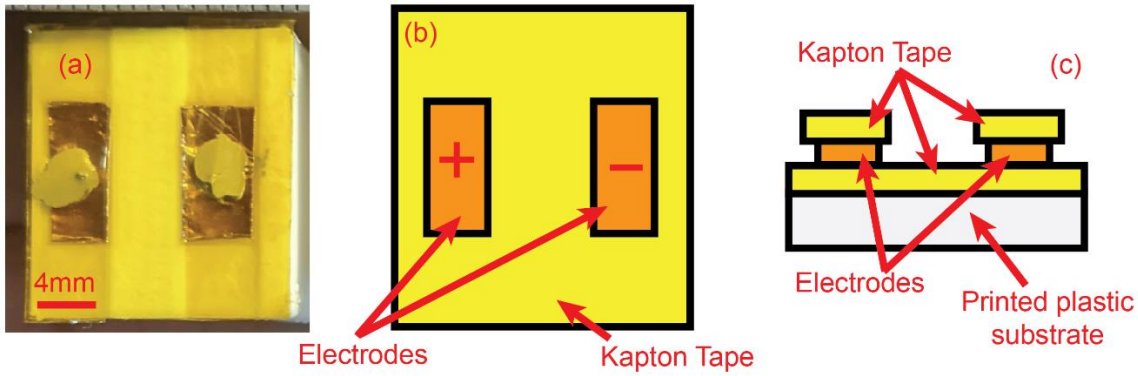


*Fig. 22 – (a) Face-on photograph of a biased Kapton target, showing white droplets of conducting epoxy used to connect the electrodes to the coaxial lines; (b) face-on diagram of the target; (c) side-on diagram of the target.*

The voltage on each electrode is maintained by individual coaxial lines. The negative electrode (emitter) is held at a voltage between -20 V and -150 V via the circuit shown in Fig. 23. The function of the capacitor on the bias side is to maintain the bias voltage on the emitter on the timescale of the discharge. The positive electrode (collector) is held at ground. The function of the inductively coupled monitor shown in the figure is to indicate the qualitive trend in the current into the collector as a function of time, whilst keeping the impedance of the path from the collector to ground as low as possible – to keep the voltage on the collector at ground for the duration of the experiment. The inductively coupled monitor did not perform reliably and we intend to replace it with an active current monitor for future experiments. In addition to this upgrade, we will also add voltage monitors to both electrodes, to ensure their voltage is not significantly perturbed on the experimental timescale.

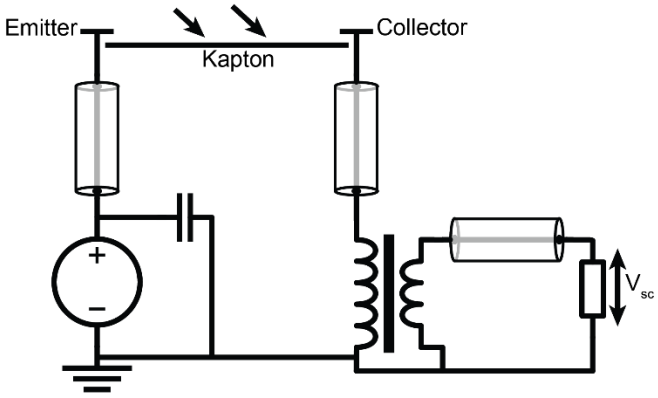


*Fig. 23 New Bias and monitoring circuitry to be used with Kapton targets in low flux experiments.*

**Optical diagnosis of low flux experiments with Kapton targets**

With the aim of providing new direct measurements of the ablation of the Kapton (and other materials) in the low fluence regime we have made a simple shadowgraphy diagnostic. This was tested in a set of experiments with Kapton targets corresponding to a radiative fluence of 100mJ/cm$^2$. Fig. 24 shows the setup:

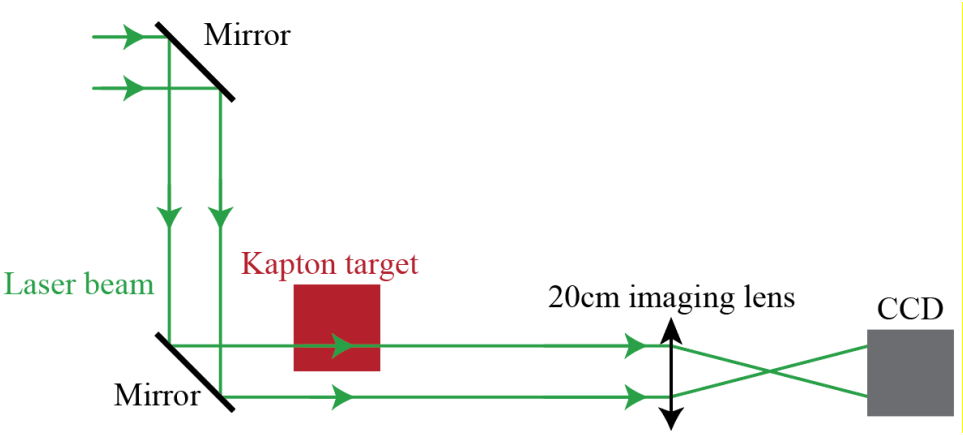


*Fig. 24 – A schematic setup of the shadowgraphy diagnostic.*

In shadowgraphy, we measure the redistribution of light due to density gradients so that the intensity in the image plane is given by

$$\frac{\Delta I}{I} = \int_0^L \left(\frac{d^2}{dx^2} + \frac{d^2}{dy^2}\right) \eta dl \ .$$

The double derivative can make it difficult to make quantitative measurements when there is experimental noise, however the minimalist approach and ease of use make shadowgraphy a natural first step for laser probing of any ablating plasma and it can be readily expanded to provide more complex probing options, including schlieren and interferometry. A collimated laser beam passes through the plasma (in this case the photo-ablated Kapton target) and is imaged using a 20cm lens and a DSLR camera. The temporal resolution of the measurement is defined by the duration of the laser pulse, 150 ps, which is much shorter than the evolution time of the plasma.

Fig. 25 shows the experimental result for a Kapton target 340 ns after current start. Comparison of a) and b) shows a clear shadowgraphy signal. Fig. 26 shows horizontal lineouts of the two images. The laser light has clearly been redistributed in the shot image, resulting in a smoother intensity gradient at the Kapton target surface.

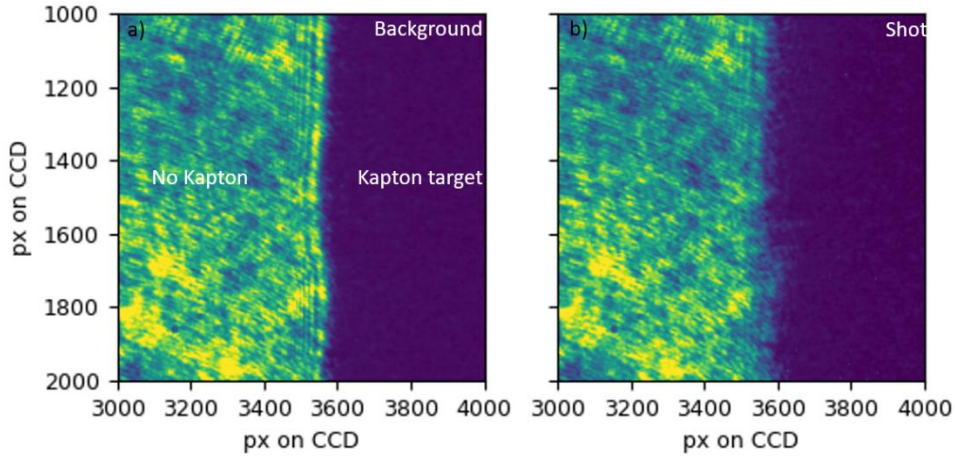


Fig. 25 – *Shadowgraphy data for a Kapton target 340 ns after current start. The light region on the left is where the laser passes the target and the dark region on the right is where the Kapton target blocks the laser. a) A background image recorded before the experiment for comparison. b) The shot shadowgram.*

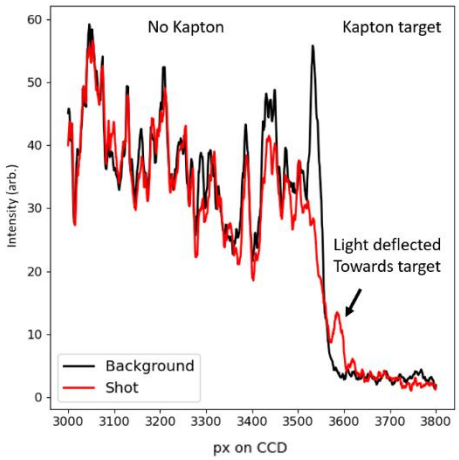


*Fig. 26 – Horizontal lineouts of intensity. The apparent deflection of light towards the target is highlighted.*

The shadowgraphy results show two things: 1. There is sufficient density that redistribution of the light in the image plane can be detected. This suggests that future laser probing diagnostics will be able to make quantitative measurements. 2. We note an increased intensity in the shot image towards the target (see label in Fig. 26).

The equation of the plasma refractive index:

$$\eta = 1 - \frac{4\pi e^2 n_e}{m_e \omega^2}$$

shows that all plasmas have a refractive index less than 1. This should result in intensity redistribution away from the target (down the density gradient), not towards the target. Deflection of light towards the target would require a neutral gas.

The possibility of a neutral gas and the demonstration that a significant variation in refractive index exists within the gas/plasma motivates further investigation with a more quantitative diagnostic. For this, we have designed a compact Mach-Zehnder interferometry diagnostic which will be built and fielded in the coming months (see Fig. 27). A similar design has been used extensively in high fluence experiments. Interferometry allows direct measurement of the refractive index (and therefore density) of a plasma (or gas) by combining a probe beam with a reference beam. We will employ two different probing wavelengths - 532 nm and 355 nm - simultaneously in the interferometer to able to distinguish between neutral and plasma density. This works because the refractive index of plasma is wavelength dependent.

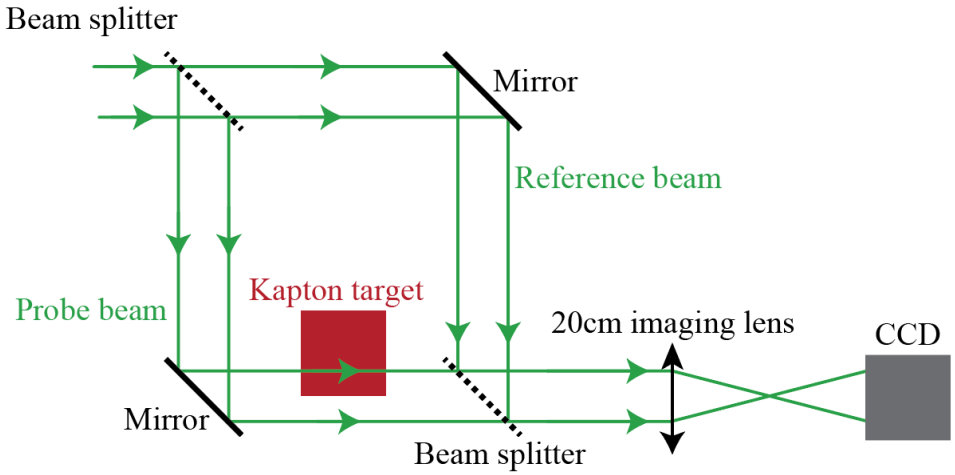


*Fig. 27 – The design for a compact Mach-Zehnder interferometer which will replace the shadowgraphy diagnostic. The optical path will be the same for both laser wavelengths.*

**Designs for an X-ray absorption diagnostics of the ablated flow**

In addition to the Chimera simulations presented in Section 4.1 have also made significant progress in simulating ablated plasma flows using the radiation-hydrodynamics code HELIOS-CR[12]. This is a 1D Lagragian hydrodynamics model and code that includes inline non-equilibrium atomic physics and radiation transport. An important feature of HELIOS-CR is the inline calculation of the plasma atomic ionization and charged state distribution using non-equilibrium atomic physics, i.e. via the self-consistent solution of a set of collisional-radiative atomic kinetic equations and the radiation transport equation. This means that these results are complementary to the work we have done using Chimera: HELIOS-CR is unable to treat the magnetic fields or multi-dimensional effects, but it provides a more detailed picture of the atomic physics. The insight these simulations provide is particularly relevant given our Thomson scattering data suggests that the charge state distribution is influenced by re-radiation.

The temperature, average ionization state and expansion velocity of the ablated silicon computed with HELIOS-CR at the end of the x-ray flux compare well with the experimental observations.

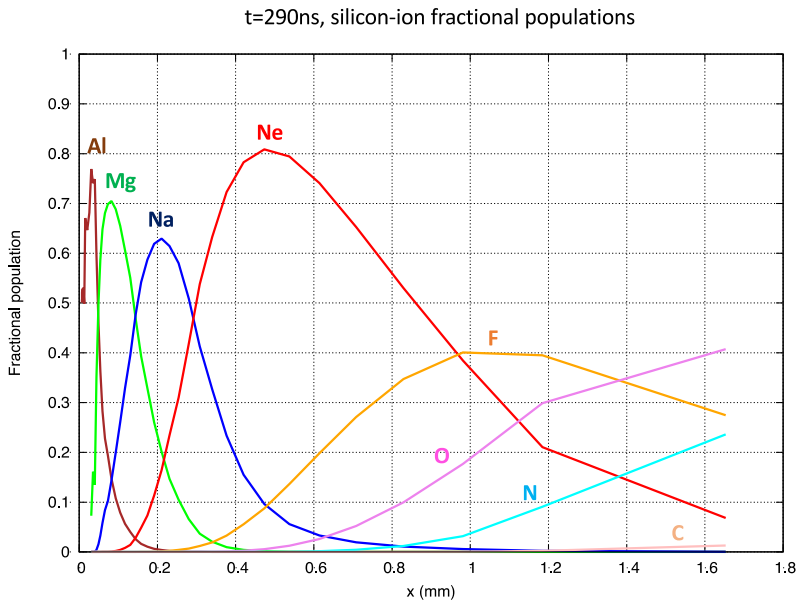


*Fig. 28: A spatial profile of the fractional populations of silicon ions.*

The figure above displays the spatial profiles of the fractional populations of silicon ions computed by HELIOS-CR at the end of the x-ray flux. The closed shell neon-like silicon peaks at about x=0.5 mm from the initial location of the silicon free surface. Further away, the silicon charged state distribution populates open-shell L-shell ions.

The calculation of the charged state distribution motivates modeling of an X-ray transmission spectrum along a line-of-sight parallel to surface of the silicon target. This is illustrated in Fig. 29. The absorption of the backlighter as it passes through the ablated plasma is collected using a spherically bent crystal spectrometer, providing one axis of spatial and one axis of spectral resolution. The spatial axis of the crystal is aligned with the direction of plasma expansion, allowing the conditions of plasma at a range of densities to be diagnosed.

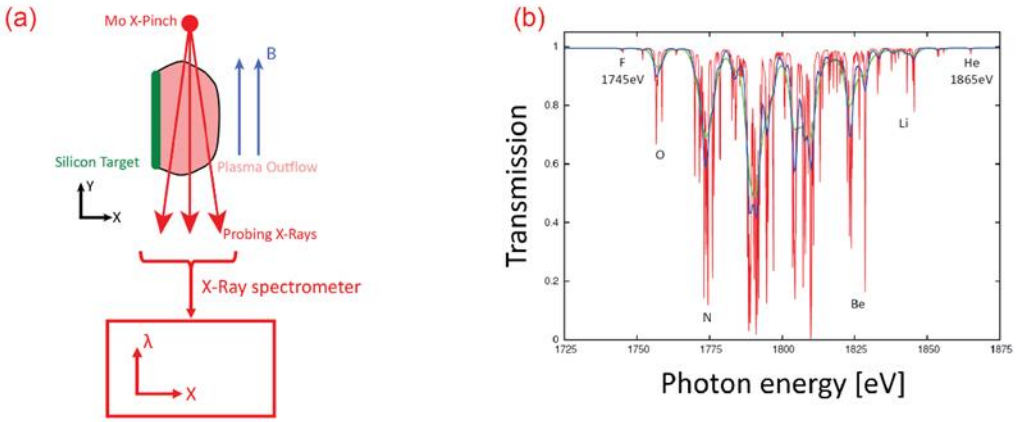


*Fig. 29: Schematic of the X-Ray absorption diagnostic; (b) synthetic spectra from a Helios-CR simulation of silicon in a high flux experiment*

Figure 29 (b) shows a synthetic absorption spectrum obtained from a Helios-CR simulation of silicon ablation in a high fluence experimental setup. The silicon K-shell absorption features which are present in the spectrum can be associated with different ionization stages of silicon and so the relative intensities can be used to back out the charge state distribution. Depending on the spectral resolution which is achievable in an experiment, the ratio of lines for a given ionization stage may also prove to be a useful diagnostic of plasma temperature.

For experiments in the high flux regime (i.e. with targets close to the pinch), backlighter radiation can be supplied by an X-Pinch driven in the return current on the MAGPIE generator – Fig. 30 shows the experimental set up in test experiments. The X-Pinch consists of a pair of crossed wires, through which an intense current pulse is driven. It emits >> 100 mJ X-Ray pulse with a duration of ~ 1 ns. The spectral character of the probe is set by the choice of wire material. If molybdenum is used then the spectrum is a smooth continuum in the 1-5 keV range.

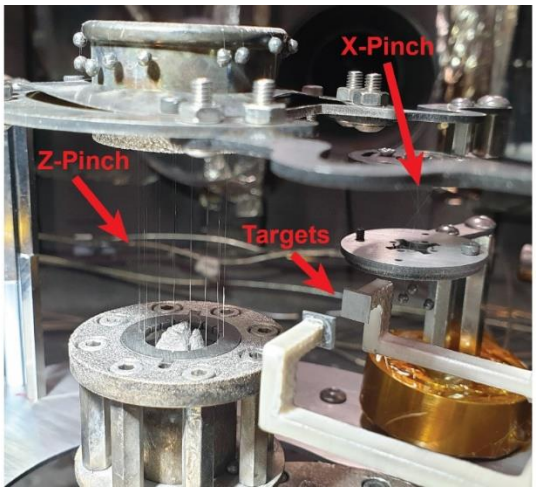


*Fig. 30 – Setup photograph of a wire array Z-Pinch in series with an X-Pinch fielded in the current return path*

Unfortunately these initial experiments were marred by breakdowns within the MAGPIE facility. Issues with the backlighter prevented any results being obtained during experiments on the Cobra facility at Cornell which we attempted to utilize whilst MAGPIE was being repaired. Meanwhile, we have explored theoretically the potential use of the diagnostic to explore any plasmas created at the surface of targets in low flux experiments. Here there is little, if any obvious ablation recorded via optical emission diagnostics (the optical framing camera), but any dense surface plasma could be sensitive to absorption probing.

Extending this diagnostic capability to low fluence experiments will require the use of a separate pulsed power generator to drive the X-Pinch – the X-pinch needs to be fielded close to the target (within cm), and so could not simply be driven in the return structure of the wire array z-pinch as planned for the high flux experiments. We have recently developed a suitable system, designed specifically to drive X-Pinches for probing external experiments[13]. A photograph of the system is shown in Fig. 31. Note that the device is very compact (largest dimension ~ 1m), can be fielded in any orientation and includes a stalk to enable the X-pinch to be inserted into other experimental

chambers. Recently the system was tested at First Light Fusion providing radiography of high speed flyer plate experiments on the Cepage facility[14].

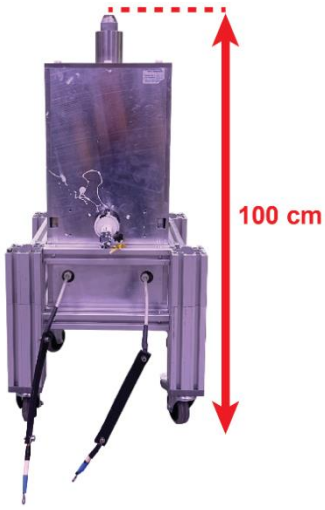


*Fig. 31 – An image of Dry Pinch I, a portable X-Pinch driver that will be used for performing absorption spectroscopy in low flux experiments*

## APPENDIX A - Publications and Presentations

All the below have used/leveraged research from the DTRA funding:

### INVITED TALKS /COLLOQIA

1. **Experimental measurements of the interaction of prompt X-rays with solar panel materials** S N Bland, Colloquium to the Materials Science for Extreme Environments University Alliance at UCSD 2021**.**

2. **Investigating magnetised, radiatively driven plasmas with a university scale pulsed-power generator** JWD Halliday, APS-DPP 2021 – invited talk

3. **Pulsed Power Z-Pinch(ish) Program at Imperial College**, S.N. Bland, ZnetUS workshop 2022 – invited talk

### CONTRIBUTED CONFERENCE PRESENTATIONS

- **Experimental Measurements of X-Ray Driven Plasma Ablation From Solid Density Silicon Targets** J W D Halliday APS-DPP 2020 – poster.

  ***

- **Diagnosis of magnetic flux penetration in radiatively driven plasma flows,** J.W.D. Halliday**,** Institute of Physics Annual Plasma Physics Conference 2022 - contributed talk.

  ***

- **Analysis of Thomson Scattering spectra obtained in experiments on the MAGPIE pulsed-power generator,** J.W.D. Halliday, High Temperature Plasma Diagnostics (HTPD) 2022 – poster.

  ****

- **A novel experimental framework for investigating colliding plasma flows with radiative cooling** , J.W.D. Halliday, High Energy Density Laboratory Astrophysics Conference (HEDLA) 2022 – contributed talk.

  ***

- **Radiatively driven plasma flows in experiments on the MAGPIE pulsed-power generator,** J.W.D. Halliday**,** International Conference on Plasma Science (ICOPS) 2022 - contributed Talk.

  ***

- **Atomic and radiative processes in X-Ray driven plasma ablation experiments performed on the MAGPIE pulsed-power generator,** J. Halliday, American Physical Society Division of Plasma Physics conference (APS-DPP) 2022 – contributed talk.

- **Recent pulsed-power driven HED plasma experiments on the MAGPIE facility**, S.V. Lebedev, American Physical Society Division of Plasma Physics conference (APS-DPP) 2022 – contributed talk.

*******

- **Investigating radiatively driven, counter-propagating plasma flows**, K. Marrow, Institute of Physics Plasma Physics meeting 2023 – poster.

  ***

- **Atomic and radiative processes in X-Ray driven plasma ablation experiments performed on the MAGPIE pulsed-power generator**, J. Halliday, International Conference on Plasma Science (ICOPS) 2023 – contributed talk.

- **Radiative instabilities in the stagnation layer of colliding, x-ray driven plasma flows**, K. Marrow, International Conference on Plasma Science (ICOPS) 2023 – poster.

## PUBLICATIONS

1. **A portable X-pinch design for x-ray diagnostics of warm dense matter**, Strucka J, Halliday JWD, Gheorghiu T, Horton H, Krawczyk B, Moloney P, Parker S, Rowland G, Schwartz N, Stanislaus S, Theocharous S, Wilson C, Zhao Z, Shelkovenko TA, Pikuz SA, Bland SN, Matter and Radiation at Extremes 7, 016901 (2022); https://doi.org/10.1063/5.0059926

2. **Investigating radiatively driven, magnetized plasmas with a university scale pulsed-power generator**, Jack W. D. Halliday, Aidan Crilly, Jeremy Chittenden, Roberto C. Mancini, Stefano Merlini, Steven Rose, Danny R. Russell, Lee G. Suttle, Vicente Valenzuela-Villaseca, Simon N. Bland, and Sergey V. Lebedev, Physics of Plasmas 29, 042107 (2022); https://doi.org/10.1063/5.0084550

## REFERENCES


[1] The starfish prime test - described in 'A Quick Look at the Technical Results of Starfish Prime' DoD Report ADA955411 - produced a belt of MeV electrons, some of which were detectable 5 years later ('The Effects of High Altitude Explosions' W. Hess, NASA document TN D-2402). Several satellites were lost due to bombardment by the electrons, including the UK's Ariel 1.

[2] S.V.Lebedev, F.N.Beg, S.N.Bland, et al, Phys. Plasmas **8,** 3734 (2001) DOI: https://doi.org/10.1063/1.1385373

[3] S.V.Lebedev, F.N.Beg, S.N.Bland, J.P.Chittenden, Dangor A.E., M.G.Haines, Phys. Plasmas **9**, 2293 (2002) DOI: https://doi.org/10.1063/1.1466466

[4] S.N.Bland, S.V.Lebedev, J.P.Chittenden, et al, Phys. Plasmas **14** 056315 (2007) DOI : https://doi.org/10.1063/1.2671940

[5] S.A. Pikuz, D.B. Sinars, T.A. Shelkovenko et al, Phys. Rev. Lett. **89** 035003-1 (2002) DOI: https://doi.org/10.1103/physrevlett.89.035003

[6] D.J. Ampleford, S.V. Lebedev, S.N. Bland, Phys. Plasmas **14**, 102704 (2007) DOI: https://doi.org/10.1063/1.2795129

[7] G.F. Swadling, S.V. Lebedev, G.N. Hall et al, Rev. Sci. Instrum. **85** 11E502 (2014) DOI: https://doi.org/10.1063/1.4890564

[8] VISRAD is a commercial code available from Prism Computational Sciences Inc: https://www.prism-cs.com/Software/VisRad/overview.html

[9] W. Rozmus et al, Phys. Rev. E **96**, 043207 (2017) DOI: https://doi.org/10.1103/PhysRevE.96.043207

[10] Details on Chimera and SpK can be found in the PhD thesis of N.Niasse " Development of a Pseudo Non-LTE model for Z-pinch simulations", Imperial College London (2012) DOI: https://doi.org/10.25560/9324

[11] M.E. Sherrill, J. Abdallah, Jr. , G. Csanak et al, Journal of Quantitative Spectroscopy and Radiative Transfer **99**, 584 (2006). DOI: https://doi.org/10.1016/j.jqsrt.2005.05.047

[12] HELIOS-CR is a commercial code available from Prism Computational Sciences Inc: https://www.prism-cs.com/Software/Helios/overview.html

[13] J. Strucka, J. W. D. Halliday, T. Gheorghiu et al, Matter and Radiation at Extremes, **7**, 016901 (2022) DOI: https://doi.org/10.1063/5.0059926

[14] J. Read, G. Burdiak, S. N. Bland et al, "Point projection radiography of electromagnetically accelerated flyer plates with an external x-pinch driver", submitted to RSI (2023)